p-ISSN 2301–4156 | e-ISSN 2460–5719

Ultrasound Probe Calibration Method of Single-Wire Phantom Using Levenberg-Marquardt Algorithm

Tri Arief Sardjono[1], Eko Mulyanto Yuniarno[2], I Made Gede Sunarya[3], I Ketut Eddy Purnama[4], Mauridhi Hery Purnomo[5], Norma Hermawan[6]

[1,6] Department of Biomedical Engineering, Institut Teknologi Sepuluh Nopember, Kampus ITS Sukolilo, Surabaya 60111 INDONESIA (email : [1]sardjono@bme.its.ac.id, [6]norma.hermawan@bme.its.ac.id)
[1,2,4,5] University Center of Excellence on Artificial Intelligence for Healthcare and Society, Institut Teknologi Sepuluh Nopember, Surabaya, 6011 INDONESIA (email: [1]sardjono@bme.its.ac.id, [2]ekomulyanto@ee.its.ac.id, [4]ketut@te.its.ac.id, [5]hery@ee.its.ac.id)
[2,4,5] Department of Computer Engineering, Institut Teknologi Sepuluh Nopember, Surabaya 60111 INDONESIA (email: [2]ekomulyanto@ee.its.ac.id, [4]ketut@te.its.ac.id, [5]hery@ee.its.ac.id)
[3] Department of Education of Informatic Engineering, Universitas Pendidikan Ganesha, Buleleng 81117 INDONESIA (email: [3]sunarya@undiksha.ac.id)

[Received: 9 March 2023, Revised: 17 July 2023]
Corresponding Author: Tri Arief Sardjono

ABSTRACT — A freehand three-dimensional (3D) ultrasound system is a method of acquiring images using a 3D ultrasound probe or conventional two-dimensional (2D) ultrasound probe to give a 3D visualization of an object inside the body. Ultrasounds are used extensively in clinical applications since they are advantageous in that they do not bring dangerous radiation effects and have a low cost. However, a probe calibration method is needed to transform the coordinate position into a 3D visualization display, especially for image-guided intervention. The current ultrasound probe calibration system usually uses the numerical regression method for the N-wire phantom, which has problems in accuracy and reliability due to nonlinear point scattered ultrasound image data. Hence, a method for ultrasound probe positional calibration of single-wire phantom using the Levenberg-Marquardt algorithm (LMA) was proposed to overcome this weakness. This experiment consisted of an optical tracking system setup, a 2D ultrasound probe with marker, an ultrasound machine, and a single-wire object in a water container equipped with a marker. The position and orientation of the marker in a 2D ultrasound probe and the marker in the water container were tracked using the optical tracking system. A 2D ultrasound probe was equipped with a marker connected wirelessly using an optical tracking system to capture the single-wire object. The resulting sequences of 2D ultrasound images were reconstructed and visualized into 3D ultrasound images using three transformations, ultrasound beam to ultrasound probe's marker, single-wire phantom position to container's marker, and the 3D visualization transformation. The LMA was used to determine the best optimization parameters for determining the exact position and representing that 3D visualization. The experiment result showed that the lowest mean square error (MSE), rotation error, and translation error were 0.45 mm, 0.25°, and 0.3828 mm, respectively.

KEYWORDS — Single-Wire Object, 2D Ultrasound Probe, Tracking System, Levenberg-Marquardt Algorithm (LMA), Freehand, Best Fit Optimization.

I. INTRODUCTION

A Three-dimensional (3D) ultrasound system is a medical imaging tool widely employed in clinical applications to acquire images of the internal object inside the body. This modality has several advantages in comparison to other 3D modalities. These advantages include cheaper, safer due to low radiation, and easier to operate. Ultrasound imaging is extensively employed in medical fields to observe and diagnose several conditions, such as prenatal diagnosis, breast imaging, digestive imaging, vascular or intra-vascular imaging, and transrectal imaging. Understanding the interpretation and how to utilize anatomical knowledge of ultrasound images is essential. The ability to interpret two-dimensional (2D) and 3D ultrasound images has become a necessary skill for medical professionals [1].

A radial ultrasound endoscope has been implemented in digestive diagnostic procedures to improve accuracy and operating flexibility. The radial ultrasound endoscope camera module offers a better image resolution [2]. Intravascular echocardiography techniques have been used to diagnose, treat, and monitor disease progression [3]. Meanwhile, intravascular ultrasound (IVUS) catheters are used for a more comprehensive assessment to guide cardiovascular intervention. An integrated distal motor has also been applied as an actuator for the IVUS catheter, providing speed consistency and high ultrasound outcomes in blood vessel imaging [4].

Ultrasound is also used in the field of brain imaging. The integration of the focused ultrasound system (FUS) with electrophysiological neuroimaging allows for high spatiotemporal resolution brain imaging. In addition, the modulated FUS has been demonstrated to achieve spatial selectivity in obtaining high-resolution electrophysiological neuroimaging [5]. It has also been investigated whether the utilization of high-frequency ultrafast ultrasound could diagnose and prevent cerebrovascular disease [6].

Nevertheless, the detection of boundaries remains challenging for the intervention and treatment using ultrasound. As observed in the previous study, transrectal ultrasound (TRUS) was utilized to segment the prostate area automatically [7]. Bladder tumor quantification and preoperative staging have also been done using the combination of 3D ultrasound and 3D surface imaging. This study has demonstrated that this combination could aid the medical staff in determining the bladder tumor and providing more information for clinical diagnosis [8]. Meanwhile, another study has found that the contrast-enhanced ultrasound sonography (CEUS) could improve the effectiveness of Takayasu arteritis diseases determination [9].

An automated breast volume scanner (ABVS) and an automated volumetric ultrasound scanner have been used for breast cancer screening to distinguish benign from malignant lesions using echogenic properties [10]. Telesonography, a new

computer-assisted ultrasound system, has been used to diagnose trauma patients in emergency conditions [11].

One of the limitations of ultrasound systems is the difficulty to show blood flow movement in either one dimension (1D) or 2D. Many methods to improve the accuracy for estimating 3D vector velocities have been observed [12]. Photoacoustic (PA) imaging combines ultrasound and short-pulses laser light to captures an object absorbing the laser light [13]. Then, freehand 3D has been used in gait analysis. The results of this study have provided a precise and noninvasive method [14]. In addition, freehand *3D* has been used to scan the carotid artery using motion tracking technology [15].

Calibration and validation play important roles in many imaging techniques, such as elastography [16]. The freehand 3D ultrasound is employed to clarify and ensure that the coordinate position in 3D space is correctly converted and displayed in 3D visualization mode. Several studies have proposed efficient calibration methods, such as the N-wire phantom [17]. In addition, many researchers have proposed a freehand approach to 3D ultrasound system. Some studies have also explicated the types of phantoms, ultrasound probes, image registration, and calibration quality assessment [18], [19]. A calibration system using actuator-assisted freehand 3D ultrasound is applied to make this system less skill-dependent [20]. An ultrasound calibration system of the arbitrary wire phantom was developed. A point-recognition method has been proposed to determine the relations between image and phantom space [21]. A combination of a phantom and a tracking stylus has been proposed. Clinical validation of 3D ultrasound for abdominal aortic aneurysm (AAA) has been done to evaluate the interoperator reproducibility. This procedure is routinely performed with a 2D ultrasound to determine aneurysm size progression [22]. Ultrasound-guided breast biopsy navigation system and a passive robotic needle holder have been developed using a ladder phantom [23]. The dataset obtained from the 2D ultrasound (B-scan image) and the real phantom object (single-wire object) position were statistically analyzed using nonlinear optimization approaches. The spatial calibration and error sensitivity calculation in ultrasound probe calibration has also been conducted employing independent general motion [24] and genetic algorithm [25].

Ultrasound probe calibration is essential in image-guided-based intervention applications such as in syringe needle insertion. Accuracy in determining the depth and position of the needle in the blood vessel is the primary factor so as not to tear the blood vessel. However, earlier research on ultrasound probe calibration for single-wire phantom was still unsatisfactory due to the relatively higher translation and rotation error. Most research conducted on the calibration of ultrasound probes used multiple wires (N-wire). At the same time, most researchers only used ordinary linear regression. Hence, research on ultrasound probe calibration for single-wire phantoms utilizing the Levenberg-Marquardt algorithm (LMA) is necessary. This paper presents a novel ultrasound probe calibration for a freehand 3D ultrasound imaging system using LMA.

There are three primary contributions of this research. The first is the development of a setup of integrated markers with a 2D ultrasound probe. The 2D ultrasound probe was equipped with markers as the reference of the motion capture camera. An optical motion capture camera would track these markers to determine the position and orientation. The second contribution is a single-wire phantom in the water container. A water container with markers was prepared for a single-wire phantom, which was then used as an object due to the position of the beam area crossing against the marker position, while the image resolution was unknown. The third is the optimization of the LMA-based iterative methods offer better accuracy and have more minor errors.

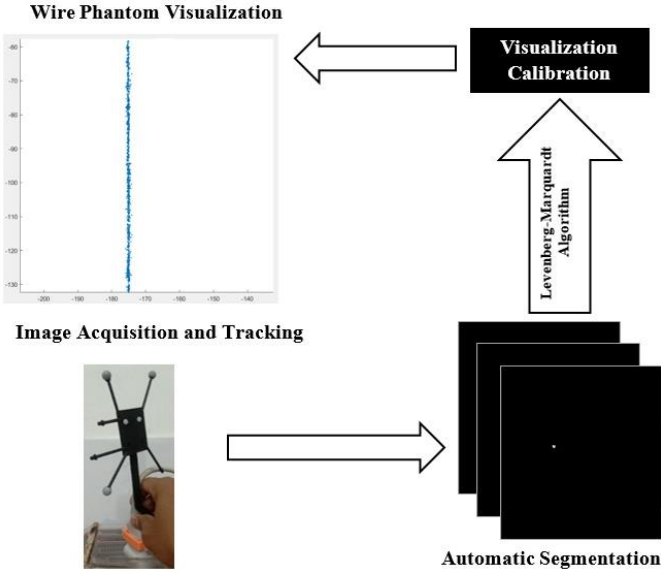

Figure 1. Proposed ultrasound single-wire phantom kalibration Process.

The state of the art of this research is the utilization of a single-wire phantom, whereas the others employed N-wire. The use of LMA in the ultrasound probe calibration method for single-wire phantom is a novel approach because it takes into account the nonlinear characteristics of the data. Most of the ultrasound probe calibration methods used a regular linear regression method.

This paper consists of several sections. The first section provides an overview of the implementation of ultrasound systems and the use of a freehand 3D ultrasound system, including a probe calibration process. The subsequent section elucidates an experimental setup for acquiring ultrasound image sequences using optical tracking. Furthermore, the transformation from tracking coordinates to phantom coordinates and the representation of rotational transformation using 3D vectors is described afterward. Finally, experimental results with a single-wire phantom are presented and discussed, followed by the conclusion of the research conducted.

II. METHODOLOGY

This section describes the proposed method for the calibration processes of the ultrasound single-wire phantom. It consists of three subsections: setup for the ultrasound single-wire phantom calibration process, transformation of B-mode coordinates to phantom coordinates, and calibration process of the system.

A. SETUP FOR ULTRASOUND SINGLE-WIRE PHANTOM CALIBRATION PROCESS

The proposed ultrasound single-wire phantom calibration process can be divided into three parts: image acquisition and tracking, single-wire phantom ultrasound images, and minimization of nonlinear least squares curve fitting problems using LMA. Figure 1 shows the proposed calibration process of ultrasound single-wire phantom.

p-ISSN 2301–4156 | e-ISSN 2460–5719

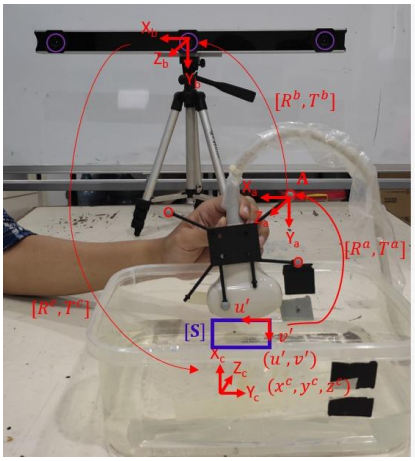

Figure 2. Setup for Ultrasound probe calibration using single-wire phantom.

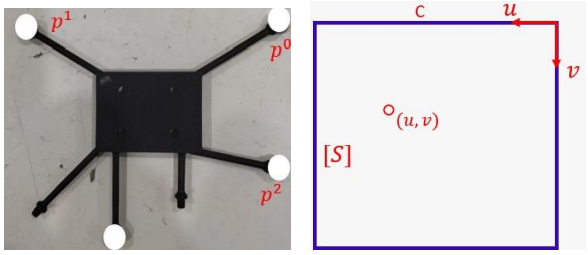

(a) (b)

Figure 3. Images of (a) an ultrasound probe marker and (b) a space coordinate system.

A setup of an ultrasound single wire phantom calibration process was developed. It consisted of a Telemed SmartUS PC based ultrasound system, 2D ultrasound linear probe of 7.5–15 MHz with markers, OptiTrack tracking system, and a single wire phantom in the water container with markers. Echo-Wave II ultrasound application was used to acquire the single wire phantom. At the same time, a nonlinear approach using LMA application was developed for the calibration process. Figure 2 shows a setup for the ultrasound single-wire phantom calibration using a 2D ultrasound probe. The marker coordinate labeled as A [X_a, Y_a, Z_a] and had three pointers.

The blue-line box labeled with S[u,v] represents the space coordinate of the single wire. Figure 2 shows the setup for ultrasound probe calibration using a single-wire phantom. The marker was attached to the ultrasound probe and followed its the movement. These markers consisted of three-pointers labeled as p^1, p^2, and p^3, representing the B-mode coordinate system.

Several coordinate systems were created based on this setup: B-mode coordinate system, phantom coordinate system, and tracking system coordinate. The B-mode coordinate system is an ultrasound beam image capture region. Several transformations are required from each coordinate system to ascertain the exact single-wire phantom position in real coordinate to image plane coordinate. Figure 3 shows the ultrasound probe marker and space coordinate system.

B. TRANSFORMATION OF B-MODE COORDINATE TO PHANTOM COORDINATE

The rigid transformation (M_T) between the B-mode image coordinates to the single-wire phantom coordinates is shown in (1). Figure 4 shows the transformation systems needed in the ultrasound single-wire phantom calibration process.

The calibration process consists of four steps: transformation from pixel coordinate to metrics (mm)

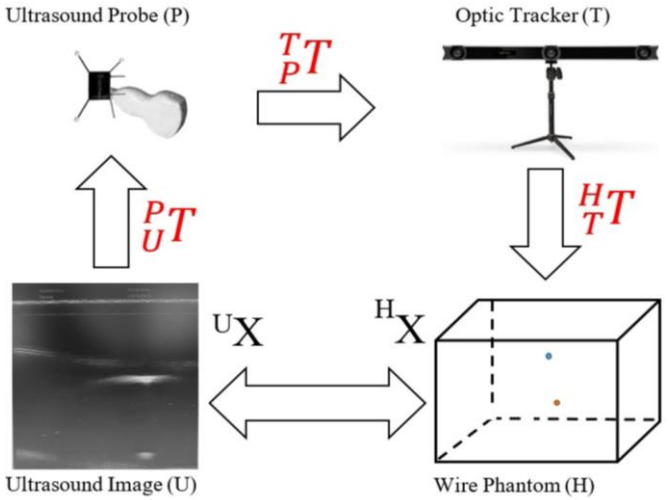

Figure 4. Transformation systems which are needed in the ultrasound single-wire phantom calibration process.

coordinate (S), the transformation from image plane coordinate to probe coordinate (M_A), the transformation from probe coordinate to tracking system coordinate (M_B), and the transformation from tracking system coordinate to phantom coordinate (M_C). Each detailed transformation will be explained in the following sections.

$$\mathbf{M}_T = \mathbf{M}_C \mathbf{M}_B \mathbf{M}_A \mathbf{S} \quad (1)$$

$\mathbf{M}_T$ = the transformation from image coordinates to 3D representation coordinates.
$\mathbf{S}$ = the transformation from pixel coordinates to metrics.
$\mathbf{M}_A$ = the transformation from (B-mode) image plane coordinates to probe coordinate.
$\mathbf{M}_B$ = the transformation from probe coordinates to the tracking system coordinates.
$\mathbf{M}_C$ = the transformation from the tracking system coordinates to 3D representation coordinate.

The coordinate system in the image plane was obtained from the probe used and in pixel units. Meanwhile, the object was in a metric unit as it was in the real or space coordinate system. Each point obtained from the B-mode image must be transformed from pixel to metric unit using (2).

$$\mathbf{S} = \begin{bmatrix} S_x & 0 & 0 & 0 \\ 0 & S_y & 0 & 0 \\ 0 & 0 & 1 & 0 \\ 0 & 0 & 0 & 1 \end{bmatrix} \quad (2)$$

with S_x and S_y are horizontal and vertical scales ratio from metric (mm) to pixel. S_x dan S_y are obtained from (3) and (4).

$$S_x = \frac{D_{mx}}{D_{px}} \quad (3)$$

$$S_y = \frac{D_{my}}{D_{px}} \quad (4)$$

where
D_{mx} = the image width (metric unit)
D_{px} = the image width (pixel unit)
D_{my} = the image length (metric unit)
D_{px} = the image length (pixel unit).

The movement of the ultrasound probe was tracked based on the marker's position and orientation. A transformation from the image plane is required to determine the precise

p-ISSN 2301–4156 | e-ISSN 2460–5719

coordinate position of a single-wire phantom object in the image plane.

1) TRANSFORMATION OF MATRIX $\mathbf{M}_A$

$\mathbf{M}_A$ is the transformation matrix from image plane coordinate to probe coordinate consisting of $\mathbf{R}^a$ and $\mathbf{T}^a$. It is represented as a matrix in (5)

$$\mathbf{M}_A = \begin{bmatrix} \mathbf{R}^a & \mathbf{T}^a \\ \mathbf{0} & 1 \end{bmatrix} \quad (5)$$

with

$$\mathbf{R}_a = \begin{bmatrix} r_1 & r_2 & r_3 \\ r_4 & r_5 & r_6 \\ r_7 & r_8 & r_9 \end{bmatrix} \quad (6)$$

and

$$\mathbf{T}^a = [t_x \quad t_y \quad t_Z\,]. \quad (7)$$

$\mathbf{R}^a$ and $\mathbf{T}^a$ are the origin and orientation of B-mode image. $\mathbf{M}_A$ is resulted from the substitution process of (6) and (7) to (5) as shown in (8).

$$\mathbf{M_A} = \begin{bmatrix} r_1 & r_2 & r_3 & t_x \\ r_4 & r_5 & r_6 & t_y \\ r_7 & r_8 & r_9 & t_z \\ 0 & 0 & 0 & 1 \end{bmatrix}. \quad (8)$$

2) DETERMINATION OF $\mathbf{M}_B$ AND $\mathbf{M}_C$ MATRIX

Local coordinate systems based on three points were the coordinate system created from three markers that were attached to the ultrasound probe. Three points $\boldsymbol{p_0}$, $\boldsymbol{p_1}$, and $\boldsymbol{p_2}$ represent the marker position and form a plane in reference coordinates. The position $\boldsymbol{p_0} = [\boldsymbol{x_0} \quad \boldsymbol{y_0} \quad \boldsymbol{z_0}]^{\boldsymbol{T}}$, $\boldsymbol{p_1} = [\boldsymbol{x_1} \quad \boldsymbol{y_1} \quad \boldsymbol{z_1}]^{\boldsymbol{T}}$ and $\boldsymbol{p_2} = [\boldsymbol{x_2} \quad \boldsymbol{y_2} \quad \boldsymbol{z_2}]^{\boldsymbol{T}}$ lied on the reference coordinate system. A local coordinate system was required with an origin $\boldsymbol{p_0}$ that had an x-axis in the same direction as the vector $\overline{\boldsymbol{p_0 p_1}}$ and the z-axis, which was perpendicular to the planes $\boldsymbol{p_0}$, $\boldsymbol{p_1}$, and $\boldsymbol{p_2}$. The vectors $\boldsymbol{v_x}$, $\boldsymbol{v_y}$, and $\boldsymbol{v_z}$ had the same direction as the local coordinate's x, y, and z-axis, so the local coordinate's position and orientation to the reference coordinate system can be calculated based on (9) until (15).

Unit vector $\boldsymbol{v_x}$ has the same direction as the vector $\overline{\boldsymbol{p_0 p_1}}$, and was obtained from (9).

$$\mathbf{v}_x = \frac{\overline{\mathbf{p_0 p_1}}}{|\overline{\mathbf{p_0 p_1}}|}. \quad (9)$$

The unit vector $\mathbf{v}_z$ was perpendicular to $\mathbf{p}_0$, $\mathbf{p}_1$, $\mathbf{p}_2$ planes and obtained from (10).

$$\mathbf{v}_z = \frac{\overline{\mathbf{p_0 p_1}} \times \overline{\mathbf{p_0 p_2}}}{|\overline{\mathbf{p_0 p_1}} \times \overline{\mathbf{p_0 p_2}}|} \quad (10)$$

$\mathbf{v}_z$ was orthonormal to v_x and v_z in the y-axis direction, so $\mathbf{v}_y$ can be obtained by applying cross product, as shown in (11).

$$\mathbf{v}_y = \mathbf{v}_z \times \mathbf{v}_x \quad (11)$$

with $\mathbf{v}_x = [v_{x1} \quad v_{x2} \quad v_{x3}]^T$, $\mathbf{v}_y = [v_{y1} \quad v_{y2} \quad v_{y3}]^T$ and $\mathbf{v}_z = [v_{z1} \quad v_{z1} \quad v_{z3}]^T$.

The orientation matrix $\mathbf{R}$ was obtained from (6) to (8), shown in (12).

$$\mathbf{R} = [\mathbf{v}_x \quad \mathbf{v}_y \quad \mathbf{v}_z] \quad (12)$$

where

$$\mathbf{T} = p_0 \quad (13)$$

Equation (13) is the local coordinate system's origin for the reference of the coordinate system.

A transformation matrix from the local coordinate system to the reference of the coordinate system $\mathbf{M}$ was obtained from (10) and (11), as shown in (14) and (15).

$$\mathbf{M} = \begin{bmatrix} \boldsymbol{R} & \mathbf{T} \\ \mathbf{0} & 1 \end{bmatrix} \quad (14)$$

$$\mathbf{M} = \begin{bmatrix} v_{x1} & v_{y1} & v_{z1} & x_0 \\ v_{x2} & v_{y2} & v_{z2} & y_0 \\ v_{x3} & v_{y3} & v_{z2} & z_0 \\ 0 & 0 & 0 & 1 \end{bmatrix} \quad (15)$$

The position and orientation of the probe to the tracking system were marked using three markers attached to the probe. If each of the three markers lays at a point $p_0^b = [\mathbf{x_0^b} \quad \mathbf{y_0^b} \quad \mathbf{z_0^b}]^{\mathbf{T}}$, $\boldsymbol{p}_1^b = [\mathbf{x_1^b} \quad \mathbf{y_1^b} \quad \mathbf{z_1^b}]^{\mathbf{T}}$ and $p_2^b = [\mathbf{x_2^b} \quad \mathbf{y_2^b} \quad \mathbf{z_2^b}]^{\mathbf{T}}$ as measured by the tracking system. The position and orientation of the probe were obtained by implementing the (17), (18), and (19) at points p_0^b, p_1^b, and p_2^b to find $\mathbf{v}_x^b.\mathbf{v}_y^b$, and $\mathbf{v}_z^b$, which were the unit vectors of the x, y, and z-axis coordinate systems of the probe. After that procedure, the probe orientation matrix to the tracking system coordinates was obtained.

$$\mathbf{R}^b = [\mathbf{v}_x^b \quad \mathbf{v}_y^b \quad \mathrm{v}_z^b] \quad (16)$$

with $\mathbf{v}_x^{\mathbf{b}} = [v_{x1}^b \quad v_{x2}^b \quad v_{x3}^b]^T$, $\mathbf{v}_y = [v_{y1}^b \quad v_{y2}^b \quad v_{y3}^b]^T$, and $\mathbf{v}_z = [v_{z1}^b \quad v_{z1}^b \quad v_{z3}^b]^T$.

Therefore, p_0 was selected as the origin of the local probe coordinate system.

$$\mathbf{T}^b = \mathbf{p}_0^{\mathbf{b}}. \quad (17)$$

Using the calculation from (14) and (15), the transformation of the probe coordinate system into a tracking system coordinate was determined using (18).

$$\mathbf{M}_B = \begin{bmatrix} \mathbf{R}^b & \mathbf{T}^b \\ 0 & 1 \end{bmatrix} \quad (18)$$

or

$$\mathbf{M_B} = \begin{bmatrix} v_{x1}^b & v_{y1}^b & v_{z1}^b & x_0^b \\ v_{x2}^b & v_{y2}^b & v_{z2}^b & y_0^b \\ v_{x3}^b & v_{y3}^b & v_{z2}^b & z_0^b \\ 0 & 0 & 0 & 1 \end{bmatrix} \quad (19)$$

The proposed phantom system consisted of a water container and a single wire. Three markers were attached to a water container which was located at $\boldsymbol{p_0^c} = [\boldsymbol{x_0^c} \quad \boldsymbol{y_0^c} \quad \boldsymbol{z_0^c}]^{\boldsymbol{T}}$, $\boldsymbol{p_1^c} = [\boldsymbol{x_1^c} \quad \boldsymbol{y_1^c} \quad \boldsymbol{z_1^c}]^{\boldsymbol{T}}$ and $\boldsymbol{p_2^c} = [\boldsymbol{x_2^c} \quad \boldsymbol{y_2^c} \quad \boldsymbol{z_2^c}]^{\boldsymbol{T}}$.

The position and orientation of the phantom coordinate system to the tracking system coordinate were determined by substituting (7) and (9) into p_0^c, p_1^c, and p_2^c. At the same time, they were also used to find unit vectors $\mathbf{v}_x^c.\mathbf{v}_y^c$ and $\mathbf{v}_z^c$, which had the same direction with x, y, and z-axis of the phantom coordinate system. Afterward, the matrix of the orientation probe $\mathbf{R}^c$ was obtained from (20).

$$\mathbf{R}^c = [\mathbf{v}_x^c \quad \mathbf{v}_y^c \quad \mathrm{v}_z^c] \quad (20)$$

with $\mathbf{v}_x^{\mathbf{c}} = [v_{x1}^c \quad v_{x2}^c \quad v_{x3}^c]^T$, $\mathbf{v}_y = [v_{y1}^c \quad v_{y2}^c \quad v_{y3}^c]^T$, and $\mathbf{v}_z^{\mathbf{c}} = [v_{z1}^c \quad v_{z1}^c \quad v_{z3}^c]^T$.

Since p_0^c was chosen as the origin of the local probe coordinate system, then

p-ISSN 2301–4156 | e-ISSN 2460–5719

$$\mathbf{T}^c = \mathbf{p}_0^c. \tag{21}$$

The transformation of the tracking system coordinate to the phantom coordinate system in (22) and (23) can be obtained from (8) or (9).

$$\mathbf{M}_C = \begin{bmatrix} \mathbf{R}^c & \mathbf{T}^c \\ 0 & 1 \end{bmatrix}^{-1} \tag{22}$$

or

$$\mathbf{M_c} = \begin{bmatrix} v_{x1}^c & v_{y1}^c & v_{z1}^c & x_0^c \\ v_{x2}^c & v_{y2}^c & v_{z2}^c & y_0^c \\ v_{x3}^c & v_{y3}^c & v_{z2}^c & z_0^c \\ 0 & 0 & 0 & 1 \end{bmatrix}^{-1}. \tag{23}$$

The matrix of coordinate tracking system to 3D representation of M_C had an opposite direction, so that an inverse was needed to find the $\mathbf{M_c}$ value.

C. CALIBRATION OF ACQUISITION SYSTEM

Since $\mathbf{S}$, $\mathbf{M_B}$ and $\mathbf{M}_C$ in (1) was determined from the results of the ultrasound acquisition system, the $\mathbf{M}_A$ matrix needed to be estimated by performing a calibration system. The proposed calibration system consisted of a single-wire phantom placed parallel to the z-axis of the phantom coordinates so that it was satisfied (24).

$$\begin{aligned} x &= x_c \\ y &= y_c \end{aligned} \tag{24}$$

with x_c and y_c are constants, u_i and v_i are the phantom position in the image plane. Therefore, the calibration purpose was to find the matrix $\mathbf{M}_A$ such that u_i, v_i satisfied (25).

$$\begin{bmatrix} x_i^c \\ y_i^c \\ z_i^c \\ 1 \end{bmatrix} = \mathbf{M}_C \mathbf{M}_B \mathbf{M}_A \mathbf{S} \begin{bmatrix} u_i \\ v_i \\ 0 \\ 1 \end{bmatrix}. \tag{25}$$

The transformation from the image plane coordinates to probe coordinate $\mathbf{M}_A$ consisted of $\mathbf{R}^a$ and $\mathbf{T}^a$. $\mathbf{R}^a$ and $\mathbf{T}^a$ are the orientation and origin of the image coordinate to the probe coordinate, which is represented as a matrix in (5).

The rotational transformation is needed because the movement of a freehand ultrasound probe is not only translational but also rotational motions, moving along the surface of the body. Rodrigues' rotation formula is an efficient algorithm for rotating a vector in space. The representation of rotational transformations using 3D rotation vectors with Rodrigues equation is shown in (26).

$$\boldsymbol{R^a} = \boldsymbol{e}^{[\boldsymbol{w}]_x} = \boldsymbol{I} + \frac{\boldsymbol{sin(\theta)}}{\boldsymbol{\theta}}[\boldsymbol{w}]_{\boldsymbol{x}} + \mathbf{1} - \frac{\boldsymbol{cos(\theta)}}{\boldsymbol{\theta^2}}([\boldsymbol{w}]_{\boldsymbol{x}})^{\mathbf{2}}. \tag{26}$$

The rotation matrix $\mathbf{R}^a$ was not directly optimized because it is not independent, $\mathbf{R}$ only has three degrees of freedom (DOF); therefore, $\mathbf{R}$ must be stated as a 3-parameter relation. Given a 3D vector $\mathbf{w} = \begin{bmatrix} w_x & w_y & w_z \end{bmatrix}^T$ with

$$[\boldsymbol{w}]_x = \begin{bmatrix} 0 & -w_z & w_y \\ w_z & 0 & -w_x \\ -w_y & w_x & 0 \end{bmatrix} \tag{27}$$

and $\theta = |\mathbf{w}|$

$$r_1 = \frac{(\cos\theta - 1)\left((w_y)^2 + (w_z)^2\right)}{(\theta)^2} + 1 \tag{28}$$

$$r_2 = -\frac{w_z \sin\theta}{\theta} - \frac{w_x w_y(\cos\theta - 1)}{(\theta)^2} \tag{29}$$

$$r_3 = \frac{w_y \sin\theta}{\theta} - \frac{w_x w_z(\cos\theta - 1)}{(\theta)^2} \tag{30}$$

$$r_4 = \frac{w_z \sin\theta}{\theta} - \frac{w_x w_y(\cos\theta - 1)}{(\theta)^2} \tag{31}$$

$$r_5 = \frac{(\cos\theta - 1)((w_x)^2 + (w_z)^2)}{(\theta)^2} + 1 \tag{32}$$

$$r_6 = -\frac{w_x \sin\theta}{\theta} - \frac{w_y w_z(\cos\theta - 1)}{(\theta)^2} \tag{33}$$

$$r_7 = -\frac{w_y \sin\theta}{\theta} - \frac{w_x w_z(\cos\theta - 1)}{(\theta)^2} \tag{34}$$

$$r_8 = \frac{w_x \sin\theta}{\theta} - \frac{w_y w_z(\cos\theta - 1)}{(\theta)^2} \tag{35}$$

$$r_9 = \frac{(\cos\theta - 1)\left((w_x)^2 + (w_y)^2\right)}{(\theta)^2} + 1 \tag{36}$$

with $\theta = |\mathbf{w}|$. By substituting $r_1, r_2, r_3, r_4, r_5, r_6, r_7, r_8$, and r_9 into (6), the orientation of the mode to the $\mathbf{R}^a$ probe was obtained. The LMA was used to minimize the geometric distance to solve nonlinear least squares problems. These problems arise in the least squares curve fitting. The Jacobian matrix in (40) was used to find $\mathbf{R}^a$ and $\mathbf{T}^a$ by minimizing the objective function

$$\chi^2(\mathbf{R}^a, \mathbf{T}^a) = \mathbf{d}^T\mathbf{d} \tag{37}$$

where

$$\mathbf{d} = [d_{1x} \quad d_{1y} \quad \cdots \quad d_{mx} \quad d_{my}]^T \tag{38}$$

and

$$d_{ix} = x_c - x_i^c(\boldsymbol{u_i}, \boldsymbol{v_i}, \mathbf{R}^a, \mathbf{T}^a) \tag{39}$$

$$d_{iy} = y_c - y_i^c(u_i, v_i, \mathbf{R}^a, \mathbf{T}^a). \tag{40}$$

From (38) and (39), the Jacobian matrix was calculated as a function s_u, s_v, $\mathbf{R}^a$, and $\mathbf{T}^a$. Since the obtained $\mathbf{R}^a$ was represented in a vector $\mathbf{w}$ in (9), the Jacobian equation obtained is following (41).

$$J = \begin{bmatrix} \frac{\partial d_{1x}}{\partial w_x} & \frac{\partial d_{1x}}{\partial w_y} & \frac{\partial d_{1x}}{\partial w_z} & \frac{\partial d_{1x}}{\partial t_x} & \frac{\partial d_{1x}}{\partial t_y} & \frac{\partial d_{1x}}{\partial t_z} \\ \frac{\partial d_{1y}}{\partial w_x} & \frac{\partial d_{1y}}{\partial w_y} & \frac{\partial d_{1y}}{\partial w_z} & \frac{\partial d_{1y}}{\partial t_x} & \frac{\partial d_{1y}}{\partial t_y} & \frac{\partial d_{1y}}{\partial t_z} \\ \vdots & \vdots & \vdots & \vdots & \vdots & \vdots \\ \frac{\partial d_{nx}}{\partial w_x} & \frac{\partial d_{nx}}{\partial w_y} & \frac{\partial d_{ny}}{\partial w_z} & \frac{\partial d_{nx}}{\partial t_x} & \frac{\partial d_{nx}}{\partial t_y} & \frac{\partial d_{nx}}{\partial t_z} \\ \frac{\partial d_{ny}}{\partial w_x} & \frac{\partial d_{ny}}{\partial w_y} & \frac{\partial d_{ny}}{\partial w_z} & \frac{\partial d_{ny}}{\partial t_x} & \frac{\partial d_{ny}}{\partial t_y} & \frac{\partial d_{ny}}{\partial t_z} \end{bmatrix} \tag{41}$$

By using the Jacobian matrix in (41) as well as the residual in (39) and (40), the parameter update is shown in (42).

$$\mathbf{h} = [\mathbf{J}^T\mathbf{J} + \lambda\, diag(\mathbf{J}^T\mathbf{J})]^{-1}\mathbf{J}^T\mathbf{d} \tag{42}$$

with

$$\mathbf{h} = [h1 \quad h2 \quad h3 \quad h4 \quad h5 \quad h6]^T \tag{43}$$

for

$$\mathbf{P} = [w_x \quad w_y \quad w_z \quad t_x \quad t_y \quad t_z]^T \tag{44}$$

Then, the new transformation parameter update is the following.

$$\mathbf{P}' = \mathbf{P} + \mathbf{h} \tag{45}$$

TABLE I
CONVERGENCES PERFORMANCE

Iteration Number	MSE
1	1.806
2	1.805
3	1.472
4	0.806
5	0.450
6	0.560
⋮	⋮
20	0.560
21	0.560
22	0.560
23	0.559

$\boldsymbol{w_x, w_y, w_z}$ are used to calculate $\mathbf{R}^a$.

III. RESULT AND DISCUSSION

The calibration method was tested using synthetic data as ground truth. The synthetic data were created using the back projection from the wire position into ultrasound image-like. The $\mathbf{R}^a$ and $\mathbf{T}^a$ parameters were obtained based on (37) by minimizing the objective function using (38). This equation consisted of the difference on the x-axis and y-axis according to (39) and (40). Table I exhibits the calculation of the average error from this equation. Figure 5 shows the mean squared error (MSE) as an iteration function.

$$\mathbf{R}_g^A = \begin{bmatrix} -0.9958 & 0.0920 & 0.0082 \\ -0.0920 & -0.9958 & -0.0884 \\ 0 & -0.0888 & 1.0001 \end{bmatrix}$$

and

$$\mathbf{T}_G^a = [9.3373 - 0.5868 - 0.1945]^T.$$

$\mathbf{R}_g^A$ and $\mathbf{T}_G^a$ matrices were the transformation from the inversion of (25). Those matrices were the transformation matrices from $\mathbf{M}_C\mathbf{M}_B$. The trial data obtained by inversion of (25) becomes:

$$\begin{bmatrix} u_i \\ v_i \\ 0 \\ 1 \end{bmatrix} = T_g^{-1} \begin{bmatrix} x_i^c \\ y_i^c \\ z_i^c \\ 1 \end{bmatrix} + \begin{bmatrix} u_i^n \\ v_i^n \\ 0 \\ 1 \end{bmatrix}.$$

Variables u_i^n and v_i^n noise was 10% of the maximum data, while T_G was the transformation obtained from the whole ground. Based on Figure 5, the trial results using 1,000 synthetic data and 200 times iteration using LMA yielded a minimum MSE of 0.45 mm as in (29). Whereas, the estimation of $\mathbf{R}_L^A$ and $\mathbf{t}_L^A$ of the B-plane image's rotation and translational position to the estimation results with LMA using a single-wire phantom was obtained.

The following matrix is $\mathbf{M}_A$ which was obtained using LMA approach.

$$[\mathbf{M}_C\mathbf{M}_B]^{-1} \begin{bmatrix} x_i^c \\ y_i^c \\ z_i^c \\ 1 \end{bmatrix} = \mathbf{M}_A\mathbf{S} \begin{bmatrix} u_i \\ v_i \\ 0 \\ 1 \end{bmatrix}$$

$$\mathbf{R}_L^a = \begin{bmatrix} -0.9957 & 0.0921 & 0.0126 \\ -0.0928 & -0.9925 & -0.0801 \\ 0.0052 & -0.0809 & 0.9967 \end{bmatrix}$$

and $\mathbf{T}_L^a = [9.5829 - 0.3103 - 0.2932]^T$.

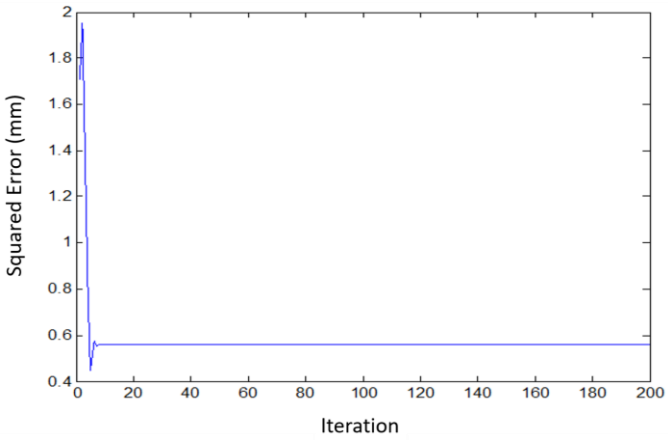

Figure 5. Mean squared error as an iteration function.

TABLE II
PERFORMANCE COMPARISON

Method	MSE	Translation Error (mm)	Rotation Error (°)
LMA	0.559	0.0106	0.25
Independent General Motion [24]	NA	69.8000	19.60
Genetic Algorithm [25]	0.500	4.9000	0.39

with an error in rotation is

$$e_r = |\mathbf{R}_L^a - \mathbf{R}_G^a| = 0.0106$$

and the error in translation is

$$e_t = |\mathbf{T}_L^a - \mathbf{T}_G^a| = 0.3828.$$

The LMA method gave superior results when compared to other methods as shown in Table II.

IV. CONCLUSION

A 3D ultrasound calibration system utilizing a single cable configuration using LMA has been proposed. An experiment was conducted with an underwater wire as a test object captured by the ultrasound imaging system. The LMA used for the calibration showed a 0.25° rotation error and 0.3828 mm translation error. Based on this method, a real-time 3D reconstruction for vascular imaging using an ultrasound system in future research will be developed.

CONFLICT OF INTEREST

Tri Arief Sardjono, Eko Mulyanto Yuniarno, I Made Gede Sunarya, I Ketut Eddy Purnama, Mauridhi Hery Purnomo, and Norma Hermawan declare that they have no conflicts of interest with any parties.

AUTHOR CONTRIBUTION

Conceptualization, Tri Arief Sardjono; methodology, Eko Mulyanto Yuniarno; formal analysis, I Made Gede Sunarya; validation, I Ketut Eddy Purnama, and Mauridhi Hery Purnomo; writing—original draft preparation, Tri Arief Sardjono, Eko Mulyanto Yuniarno and I Made Gede Sunarya; writing—review and editing, Norma Hermawan.

REFERENCES

[1] S. Allsop, S. Gandhi, N. Ridley, and M. Spear, "Implementing Ultrasound Sessions to Highlight Living Anatomy for Large Medical Student Cohorts," *Transl. Res. Anat.*, Vol. 22, pp. 1–7, Jan. 2021, doi: 10.1016/j.tria.2020.100088.

p-ISSN 2301–4156 | e-ISSN 2460–5719

[2] J. Peng *et al*., "Miniaturized High-Resolution Integrated 360° Electronic Radial Ultrasound Endoscope for Digestive Tract Imaging," *IEEE Trans. Ultrason. Ferroelectr., Freq. Control*, Vol. 66, No. 5, pp. 975–983, May 2019, doi: 10.1109/TUFFC.2019.2903308.

[3] S. Dastmalchian, H. Aryafar, and S. Tavri, "Intravascular Ultrasound Guidance for TIPS Procedures: A Review," *AJR Amer. J. Roentgenol*, Vol. 219, No. 4, pp. 634–646, Oct. 2022, doi: 10.2214/AJR.22.27626.

[4] J. Peng *et al.*, "A Novel Synchronous Micro Motor for Intravascular Ultrasound Imaging," *IEEE Trans. Biomed. Eng.*, Vol. 66, No. 3, pp. 802–809, Mar. 2019, doi: 10.1109/TBME.2018.2856930.

[5] B. He, "Focused Ultrasound Help Realize High Spatiotemporal Brain Imaging? - A Concept on Acousto-Electrophysiological Neuroimaging," *IEEE Trans. Biomed. Eng.*, Vol. 63, No. 12, pp. 2654–2656, Dec. 2016, doi: 10.1109/TBME.2016.2620983.

[6] S. Fekkes *et al.*, "Simultaneous Vascular Strain and Blood Vector Velocity Imaging Using High-Frequency Versus Conventional-Frequency Plane Wave Ultrasound: A Phantom Study," *IEEE Trans. Ultrason. Ferroelectr., Freq. Control*, Vol. 65, No. 7, pp. 1166–1181, Jul. 2018, doi: 10.1109/TUFFC.2018.2834724.

[7] Y. Wang *et al*., "Deep Attentive Features for Prostate Segmentation in 3D Transrectal Ultrasound," *IEEE Trans. Med. Imaging*, Vol. 38, No. 12, pp. 2768–2778, Dec. 2019, doi: 10.1109/TMI.2019.2913184.

[8] L. Wang and Z. Xuan, "Study on 3D Ultrasound Imaging Technology for Measuring Bladder Tumour Health Care and Information Sensing," *Meas.*, Vol. 163, pp. 1–8, Oct. 2020, doi: 10.1016/j.measurement.2020.107926.

[9] C. Zhao *et al*., "Role of Contrast-Enhanced Ultrasound Sonography in the Medical Diagnostics of the Disease Activity in Patients with Takayasu Arteritis," *IEEE Access*, Vol. 7, pp. 23240–23248, Jan. 2019, doi: 10.1109/ACCESS.2019.2896386.

[10] G.A.G.M. Hendriks, C. Chen, H.H.G. Hansen, and C.L. de Korte, "3-D Single Breath-Hold Shear Strain Estimation for Improved Breast Lesion Detection and Classification in Automated Volumetric Ultrasound Scanners," *IEEE Trans. Ultrason. Ferroelectr., Freq. Control*, Vol. 65, No. 9, pp. 1590–1599, Sep. 2018, doi: 10.1109/TUFFC.2018.2849687.

[11] M. Marsousi, K. Plataniotis, and S. Stergiopoulos, "Computer-Assisted 3-D Ultrasound Probe Placement for Emergency Healthcare Applications," *IEEE Trans. Ind. Inform.*, Vol. 12, No. 4, pp. 1380–1391, Aug. 2016, doi: 10.1109/TII.2016.2569522.

[12] S. Holbek *et al.*," Ultrasonic 3-D Vector Flow Method for Quantitative In Vivo Peak Velocity and Flow Rate Estimation," *IEEE Trans. Ultrason. Ferroelectr., Freq. Control*, Vol. 64, No. 3, pp. 544–554, Mar. 2017, doi: 10.1109/TUFFC.2016.2639318

[13] C. Lee, W. Choi, J. Kim, and C. Kim, "Three-Dimensional Clinical Handheld Photoacoustic/Ultrasound Scanner," *Photoacoustics*, Vol 18, pp. 1–8, Jun. 2020, doi: 10.1016/j.pacs.2020.100173.

[14] E. Passmore and M. Sangeux, "Defining the Medial-Lateral Axis of an Anatomical Femur Coordinate System Using Freehand 3D Ultrasound Imaging," *Gait, Posture*, Vol. 45, pp. 211–216, Mar. 2016, doi: 10.1016/j.gaitpost.2016.02.006.

[15] S. Chung, C. Shih, and C. Huang, "Freehand Three-Dimensional Ultrasound Imaging of Carotid Artery Using Motion Tracking Technology," *Ultrason.*, Vol. 74, pp. 11–20, Feb. 2017, doi: 10.1016/j.ultras.2016.09.020.

[16] N. Hermawan, T. Ishii, and Y. Saijo, "Color Doppler Shear Wave Elastography Using Commercial Ultrasound Machine with Compensated Transducer Scanning Delay," *J. Med. Ultrason.*, Vol. 49, No. 2, pp. 163–173, Apr. 2022, doi: 10.1007/s10396-022-01194-7.

[17] B. Mathieu, C. Claire, L. Lorenzo, and V. Arturo, "Temporal and Spatial Calibration of a Freehand 3D Ultrasound Reconstructions System by Using an N-Wire Phantom," *2015 12th Int. Conf. Elect. Eng. Comput. Sci., Autom. Control (CCE)*, 2015, pp. 1–7, doi: 10.1109/ICEEE.2015.7357966.

[18] Q. Huang and Z. Zeng, "A Review on Real-Time 3D Ultrasound Imaging Technology," *BioMed Res. Int.*, Vol. 2017, pp. 1–20, Mar. 2017, doi: 10.1155/2017/6027029.

[19] M.H. Mozaffari and W.S. Lee, "Freehand 3-D Ultrasound Imaging: A Systematic Review," *Ultrasound in Med., Biol.*, Vol. 43, No. 10, pp. 2099–2124, Oct. 2017, doi: 10.1016/j.ultrasmedbio.2017.06.009.

[20] T.K. Koo and N. Silvia, "Actuator-Assisted Calibration of Freehand 3D Ultrasound System," *J. Healthc. Eng.*, Vol 2018, pp. 1–11, May 2018, doi: 10.1155/2018/9314626.

[21] C. Shen, L. Lyu, G. Wang, and J. Wu, "A Method for Ultrasound Probe Calibration Based on Arbitrary Wire Phantom," *Cogent Eng.*, Vol. 6, No. 1, pp. 1–13, Apr. 2019, doi: 10.1080/23311916.2019.1592739.

[22] Q.M. Ghulam, S. Kilaru, S. Ou, and H. Sillesen, "Clinical Validation of Three-Dimensional Ultrasound for Abdominal Aortic Aneurysm," *J. Vasc. Surg.*, Vol. 71, No. 1, pp. 180–188, Jan. 2020, doi: 10.1016/j.jvs.2019.03.066.

[23] J. Suthakorn, N. Tanaiutchawoot, and C. Wiratkapan, "Ultrasound Calibration with Ladder Phantom at Multiple Depths for Breastbiopsy Navigation System," *Theor. App. Mech. Lett.*, Vol. 10, No. 5, pp. 343–353, Jul. 2020, doi: 10.1016/j.taml.2020.01.037

[24] Q. Cai *et al*., "Spatial Calibration for 3D Freehand Ultrasound via Independent General Motions," *2020 IEEE Int. Ultrason. Symp. (IUS*), 2020, pp. 1–3, doi: 10.1109/IUS46767.2020.9251558.

[25] Q. Cai *et al*., "Quantitative Study on Error Sensitivity in Ultrasound Probe Calibration with Hybrid Tracking," *2021 IEEE Int. Ultrason. Symp. (IUS*), 2021, pp. 1–4, doi: 10.1109/IUS52206.2021.9593708.